Electronic Supplementary Information

Engineering the Carrier Dynamics of g-C_3N_4 by Rolling up the Planar Sheets to Nanotubes via Ultrasonic Cavitation

Zhixing Gan,[a,b,c,*] Lizhe Liu,[c] Pengfei Pan,[a] Yawen Lin,[a] Jiancang Shen[c] and Baohua Jia[b,*]

a. Key Laboratory of Optoelectronic Technology of Jiangsu Province, School of Physics and Technology, Nanjing Normal University, Nanjing 210023, China

b. Centre for Micro-Photonics, Faculty of Science Engineering and Technology, Swinburne University of Technology, Hawthorn VIC 3122, Australia

c. National Laboratory of Solid State Microstructures, Nanjing University, Nanjing 210093, China

E-mail: zxgan@njnu.edu.cn (Z. G.); bjia@swin.edu.au (B. J.)

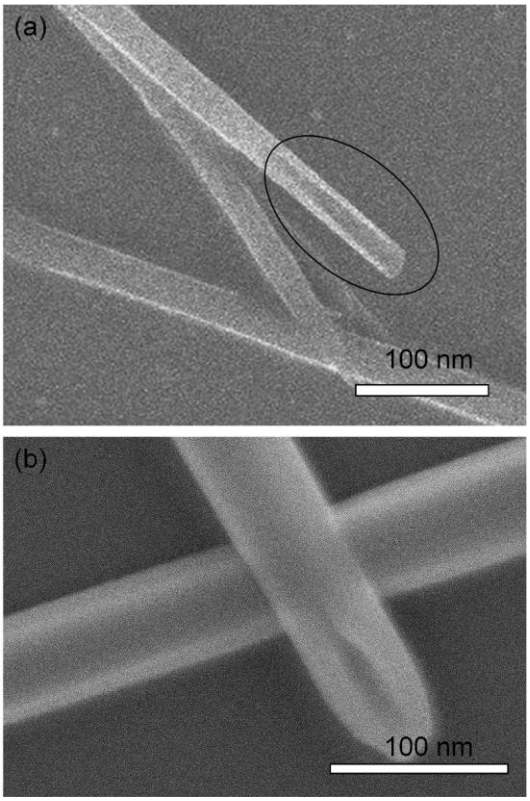

S1. SEM images of g-C_3N_4 nanotubes. (a) the black circle highlights an open end with rolled character. (b) SEM image of another g-C_3N_4 nanotube with open end.

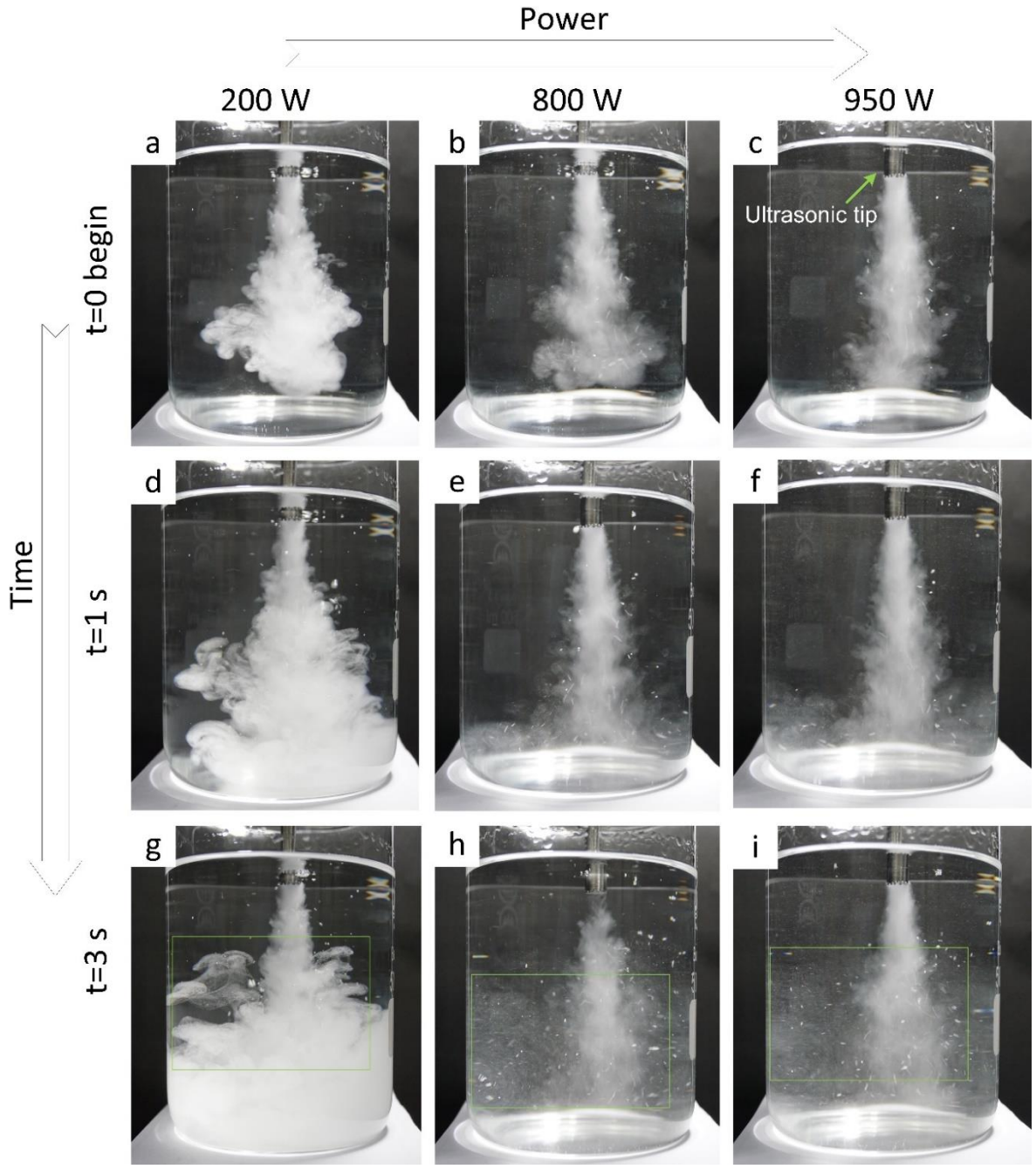

S2. Photos of the bubbles generated by probe-ultrasonications at different powers, 200 W (a,d,g), 800 W (b,e,h), and 950 W (c,f,i). The selected rectangular areas are zoomed in and displayed in **S3**.

To observe the bubbles directly, a mixture of ethanol and water without g-C_3N_4 was treated by probe-ultrasonication. When the power is 200 W, a dense fog rapidly appear in the solvent (a), indicating there are plenty of tiny bubbles. And the fog becomes bigger and denser with increasing ultrasonic time (a,d,g). In this situation, stable bubbles with lifetime longer than one second are dominant. When the power increases to 800 W, the fog is much lighter and

independent on ultra-sonic time (b,e,h). It suggests that the fraction of inertial cavitation increases tremendously. The generation and rupture of the bubbles occur within one second, which is faster than a single frame. When the power further increases to 950 W, the fog is similar to that generated at 800 W. Note when g-C_3N_4 powder was added, the solution was muddy and thus the direct observation of bubbles was failure.

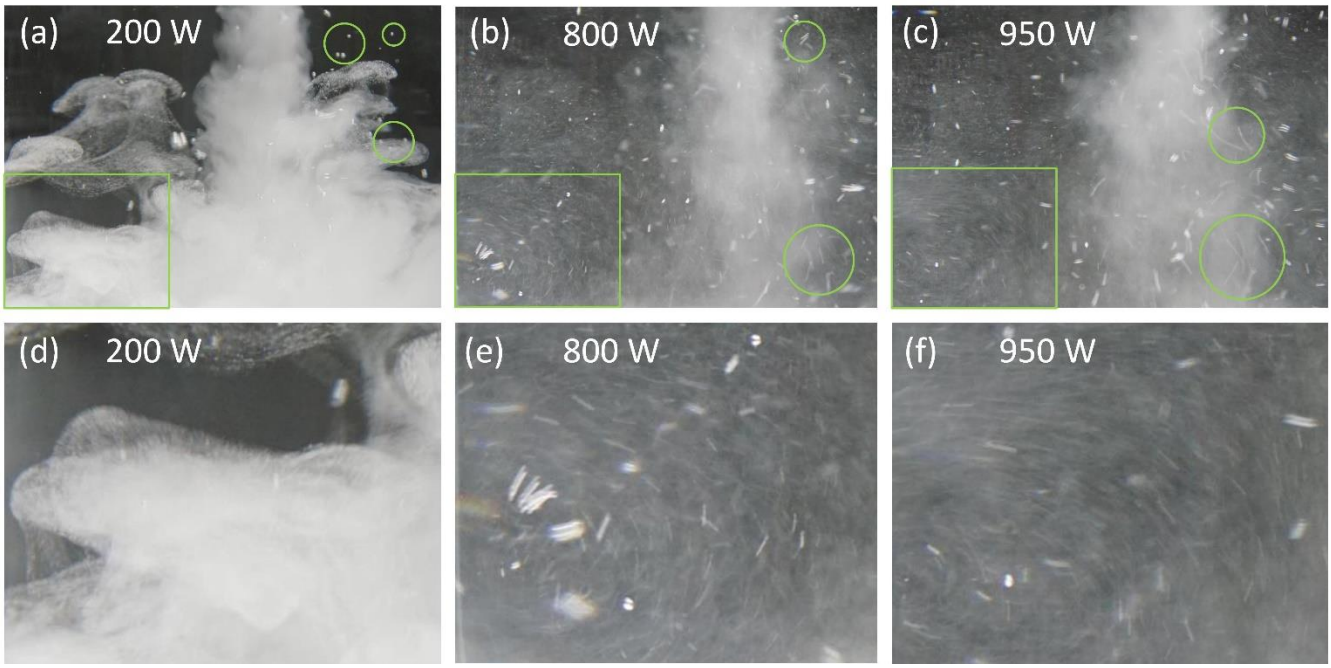

S3. (a-c) Enlarged images of the areas marked in g-h of **S2**. (d-f) The rectangular regions of a-c are further zoomed in and showed in d-f, respectively.

As highlighted by the circles in a, many stable spherical bubbles can be found at the power of 200 W. However, at the power of 800 W, the bubbles become elongated. When the ultrasonication power is 950 W, the sizes of the elongated bubbles increase evidently. In fact, these elongated bubbles are quite unstable. They explode immediately after generation. By further zooming in the rectangular area in a, crowded tiny bubbles are observed. Whereas, the enlarged image corresponding to (b) display many elongated bubbles with different sizes.

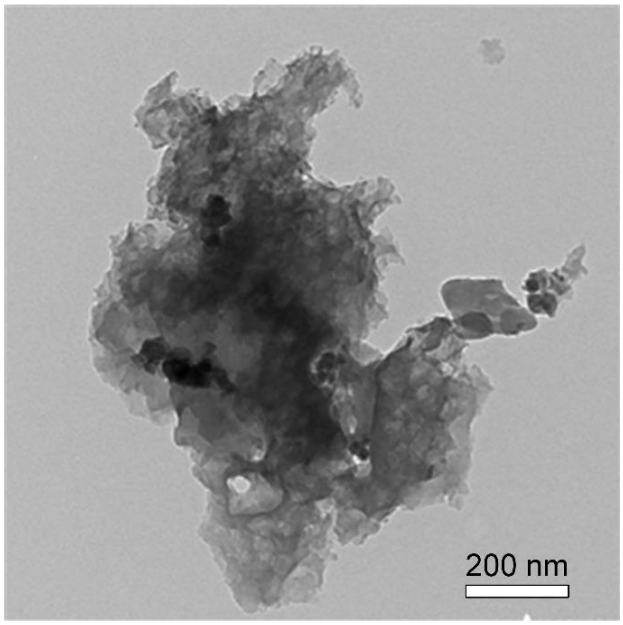

S4. TEM image of the product from 200 W probe-sonication of g-C_3N_4 powder.

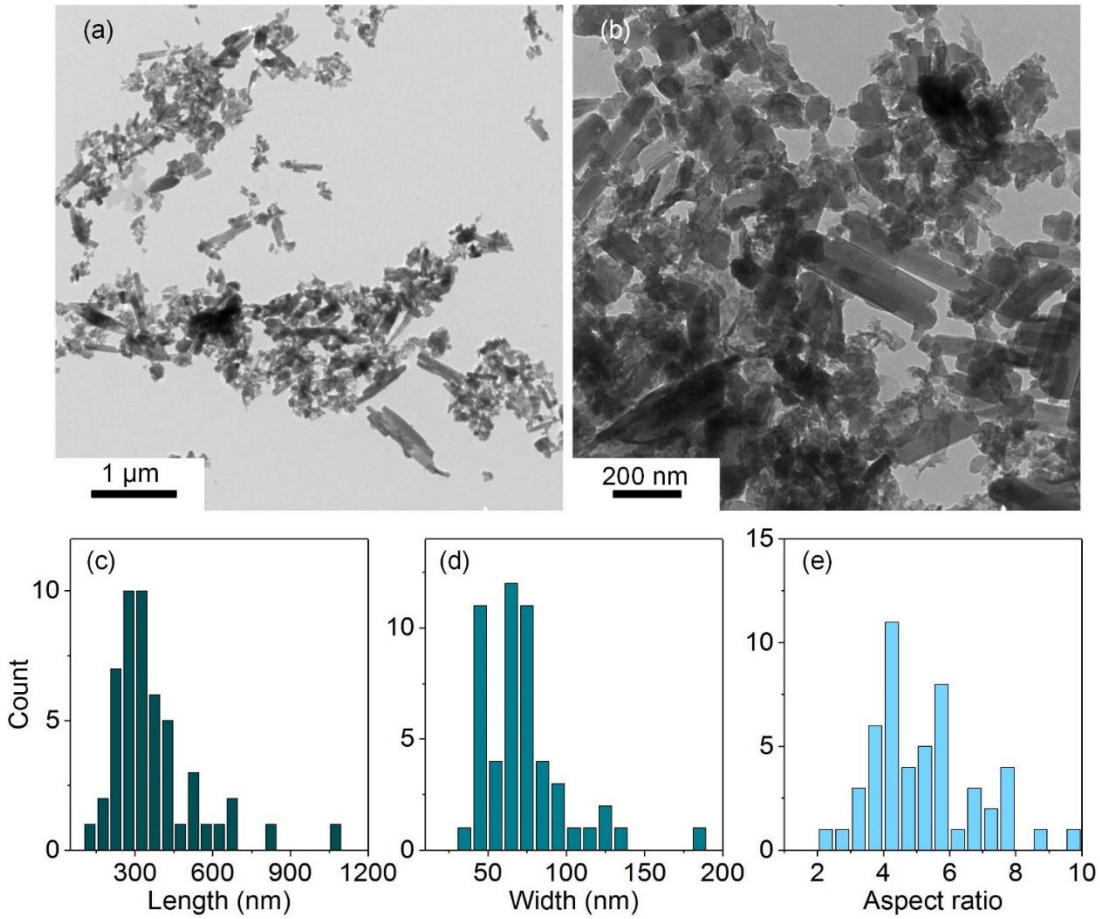

S5. (a,b) TEM images of the product fabricated by 950W probe-sonication. (c-e) Length (c), width (d) and aspect ratio (e) distributions of the nanotubes.

S6. Discussion on other 2D materials

Similar ultrasonic treatments on other 2D materials, like MoS_2,[R1] WS_2,[R2] BN,[R3] and black phosphorus[R4,R5] are widely reported. However, usually they are fractured to ultrasmall QDs due to the shear force-induced exfoliation and scission force-induced cutting. The difference may be caused by the high flexibility of g-C_3N_4. The g-C_3N_4 is composed of tri-s-triazine moieties connecting by a single C–N covalent bond, which render its corrugations and deformations easily. Previous works show that Young's modulus of planar g-C_3N_4 nanosheets is around 221.62 GPa[R6] which is evidently lower than those of graphene (1 TPa),.[R7] hexagonal BN nanosheets (250 GPa), [R8] MoS_2 (330 GPa),[R9] and WS_2 (238 GPa).[R10] Therefore, in general, corrugation stabilizes g-C_3N_4 nanostructures with respect to extended conformations in comparison to other 2D atomic layers,[R11] indicating that the curving of g-C_3N_4 sheets to nanotubes is easier.[R12] In principle, the feasibility of this method relies on the mechanical properties of the 2D materials. The g-C_3N_4 nanosheets prepared by different precursors should have similar mechanical properties. And it is logical to expect this method is versatile to other flexible 2D materials.

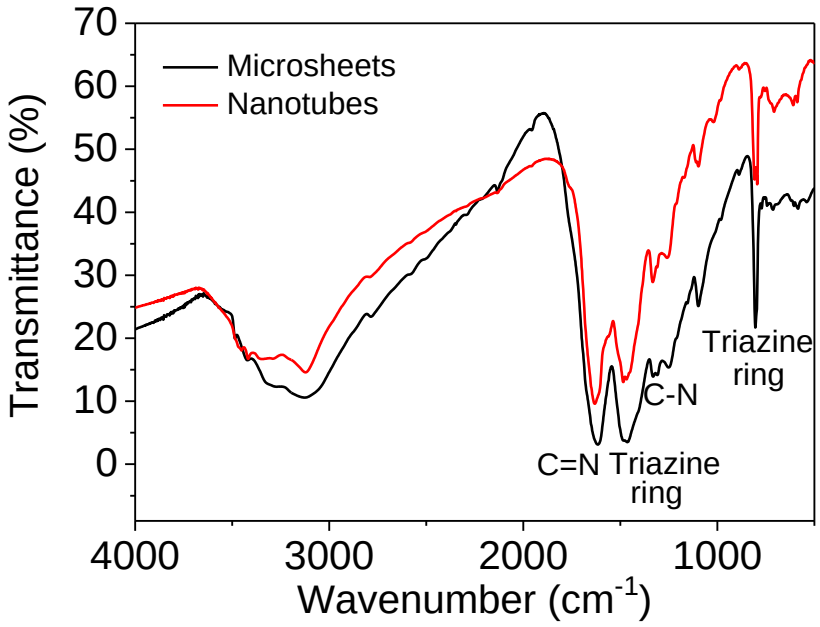

S7. FTIR spectra of g-C_3N_4 microsheets (black line) and nanotubes (red line).

Both microsheets and curved nanotubes exhibit very similar FTIR spectra, indicating the chemical composition and functional groups remain unchanged during the rolling up of planar

g-C_3N_4 to nanotubes. The wide band between 3000 and 3600 cm^{-1} corresponds to the stretching vibration mode of residual NH_2, NH groups at the defect sites of the aromatic ring and also possibly stretching mode of OH.[R13,R14] The strong band locating at 1620 cm^{-1} is associated with the typical stretching and rotation vibration of C=N.[R13,R14] The other strong peak at 1490 cm^{-1} belongs to tri-s-triazine ring modes.[R13,R14] Besides, the band at 805 cm^{-1} also corresponds to the breathing mode of the heptazine ring arrangement. The bands in the 1000-1350 cm^{-1} region are ascribed to the C–N stretchings.[R13,R14]

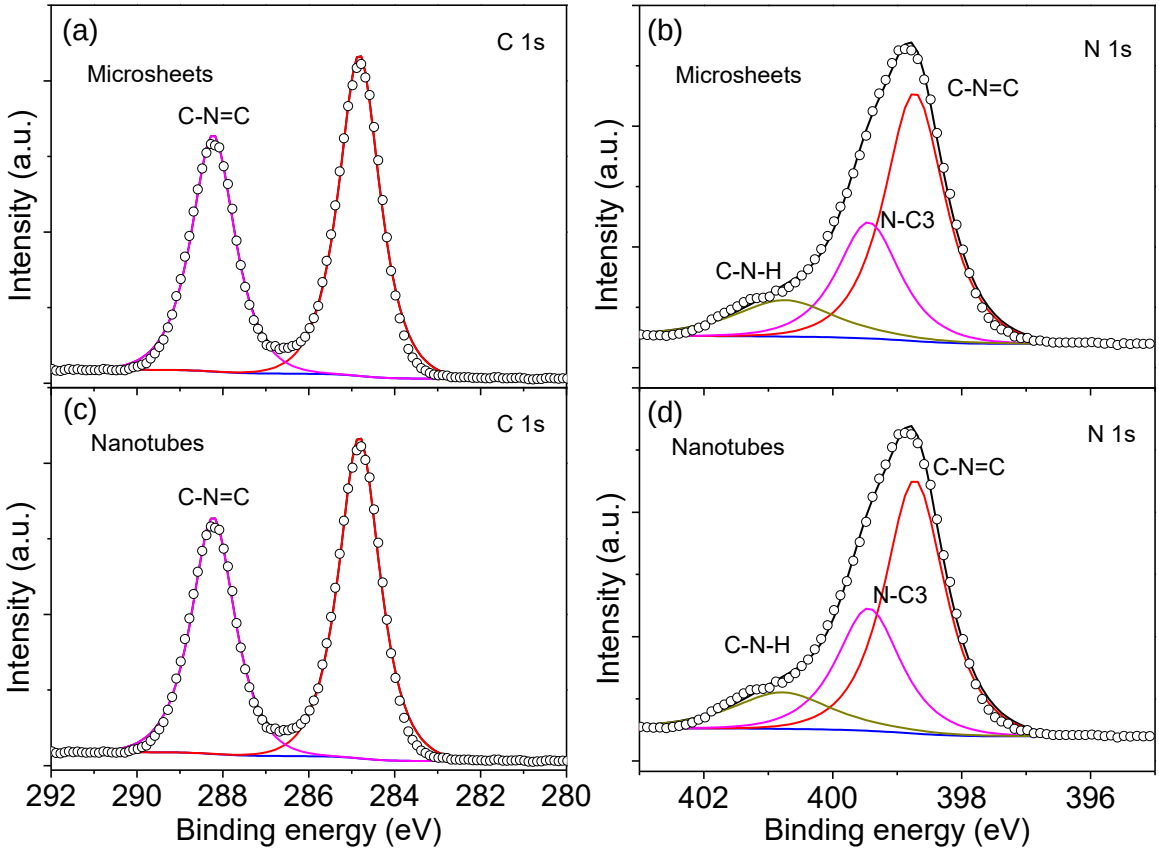

S8. X-ray photoelectron spectra (XPS) of C 1s (a,c) and N 1s (b,d).

The C 1s spectra for both microsheets and nanotubes can be fitted into two peaks, centered at 284.8 and 288.2 eV (Fig. 5c), which are ascribed to sp^2 –C=C– bonds and sp^2-hybridized carbon of C–N=C coordination, respectively.[R15-R20] The N 1s spectra are deconvoluted into three sub-bands. The peak at 398.6 eV is ascribed to sp^2-hybridized aromatic nitrogen atoms bonded to carbon atoms (C–N=C). The second one at 399.4 eV belongs to the tertiary N– (C)3 groups. And the third peak assigning to the N bonded with H atoms (C–N–H) is found at 400.8 eV.[R15-R20] Overall, the XPS spectra of microsheets and nanotubes are almost the same, further

suggesting the chemical states and atomic structures of g-C_3N_4 microsheets and nanotubes are nearly the same.

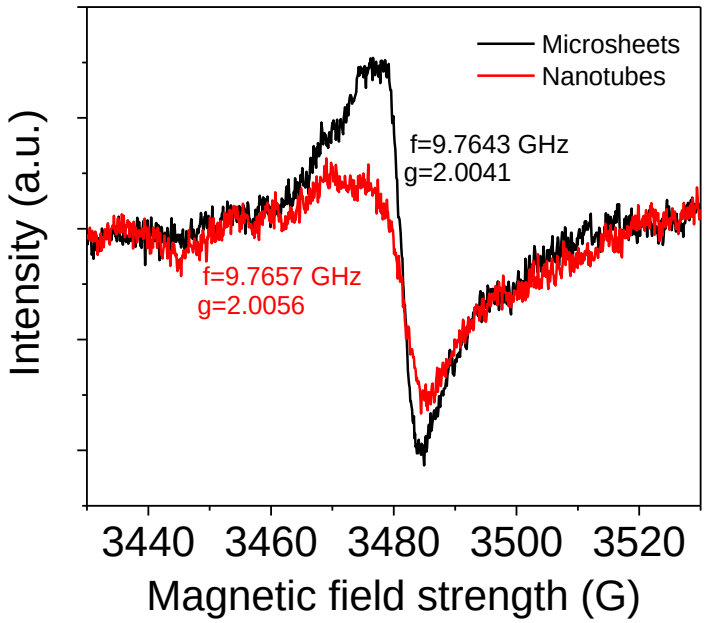

S9. EPR spectra of g-C_3N_4 microsheets (black line) and nanotubes (red line).

EPR spectra of both samples exhibit a single Lorentzian line in the magnetic field from 3440 to 3530 G. The g values of g-C_3N_4 microsheets and nanotubes are calculated as 2.0041 and 2.0056. According to the literature, EPR signal is associated with the unpaired electrons of sp^2-carbon atoms within π-conjugated aromatic rings.[R20,R21] For example, the two-coordinated nitrogen vacancies may donate unpaired electrons to adjacent sp^2-carbon atoms within π-conjugated aromatic rings in g-C_3N_4.[R21] The intensities of EPR signals are very close indicating the density of atomic vacancies retains in g-C_3N_4 nanotubes. However, the divergence of g values implies the unpaired electron must have gained or lost angular momentum through spin–orbit coupling due to the change of the shapes.

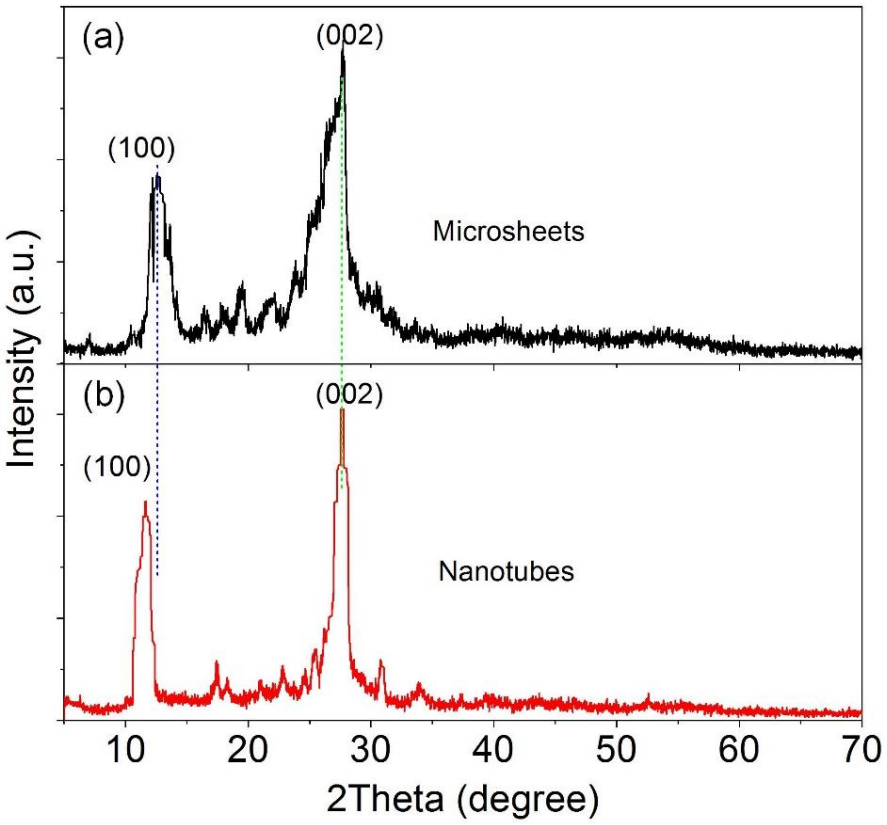

S10. XRD patterns of g-C_3N_4 microsheets (a) and nanotubes (b). The broad and noised peak imply the poor crystallinity, which is in good agreement with the SAED result.

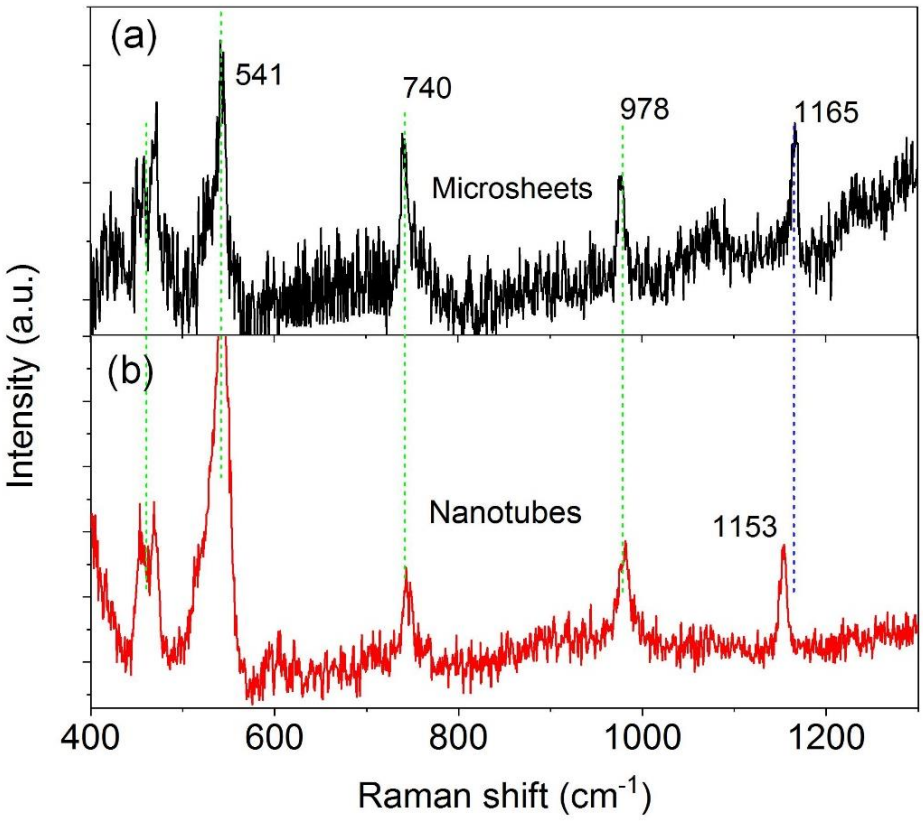

S11. Raman spectra of g-C_3N_4 microsheets (a) and nanotubes (b) after background and offset corrections.

A 785 nm laser was used as the excitation source to avoid the strong fluorescent background. The peaks at 541 and 740 cm^{-1} are ascribed to the twisting vibration and in-plane symmetrical stretching vibration of heptazine heterocycles, respectively.[R19] And the 978 cm^{-1} band is associated with the breathing modes of the heptazine ring.[R20] These three modes (541, 740, and 978 cm^{-1}) appear at same positions in the Raman spectra of g-C_3N_4 microsheets and nanotubes. However, the peak at 1165 cm^{-1} shifts toward lower frequencies after the microsheets are rolled up to nanotubes. This peak is ascribed to the =C(sp^2) bending vibration, depending on the C–N covalent bonds.[R19] The redshift of this mode suggests the C–N bonds are stretched. Similar Raman redshift caused by the elongation of C–C bond also exists in strained graphene, which show shifts of ca. 27.8 and 14.2 cm^{-1} per 1% strain in 2D and G band, respectively.[R21]

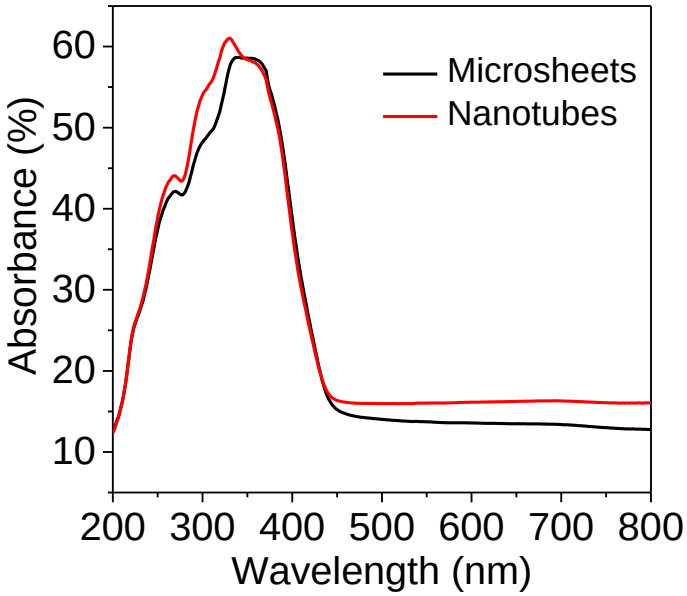

S12. Absorption spectra of g-C_3N_4 microsheets (black line) and nanotubes (red line). The g-C_3N_4 microsheets and nanotubes exhibit identical absorption edge at 450 nm, implying the same direct bandgap of 2.76 eV. While the absorption of nanotubes in the visible range (450-800 nm) is improved apparently, which is agreement with the steady-state PL spectra.

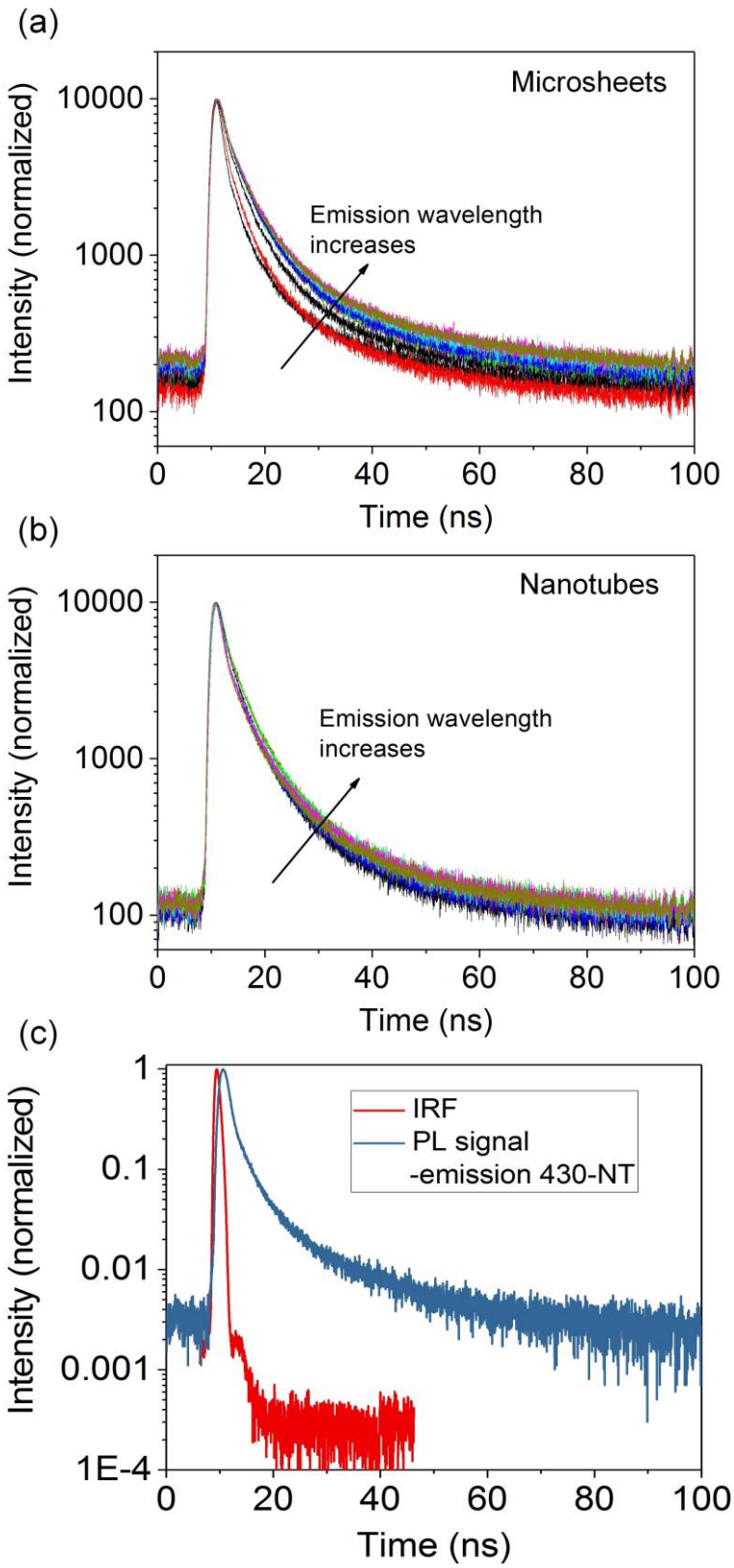

S13. (a,b)TRPL decay curves monitored at different emission wavelengths, (a) microsheets (b) nanotubes. (c) The instrumental response function (IRF) is compared with a TRPL decay curve. In our system, the IRF is much faster than TR-PL signal. Thus, the IRF has a negligible influence on the fitting parameters.

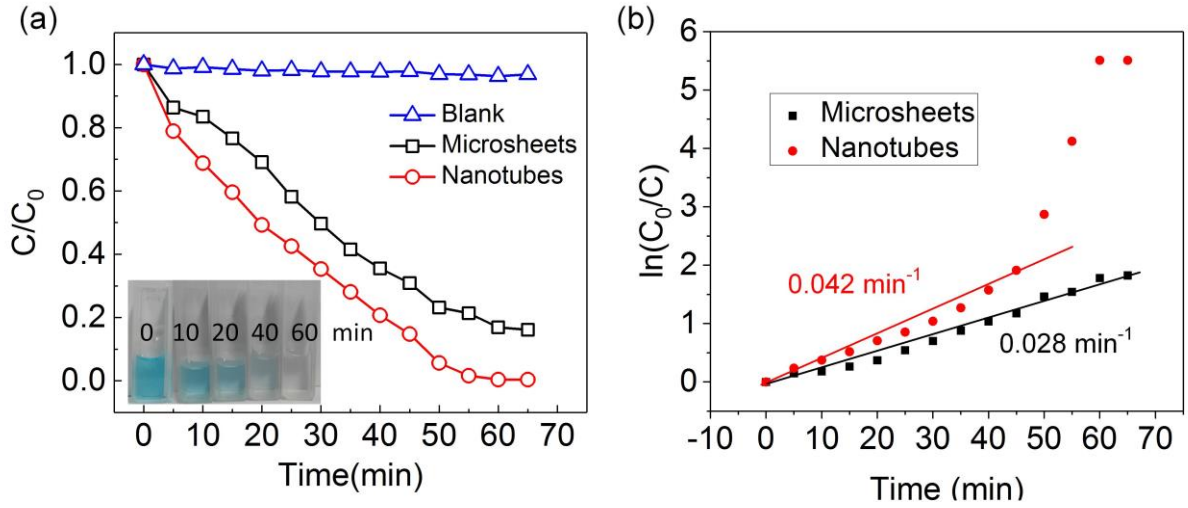

S14. (a) Photodegradation of MB over g-C_3N_4 microsheets and nanotubes under visible irradiation. (b) ln(C0/C) as a function of irradiation time (t). Contrastive experiment without any catalyst was performed for comparison (Blank), showing that the self-degradation of MB under visible light irradiation is negligible. Inset: pictures taken during degradation of MB over g-C_3N_4 nanotubes.

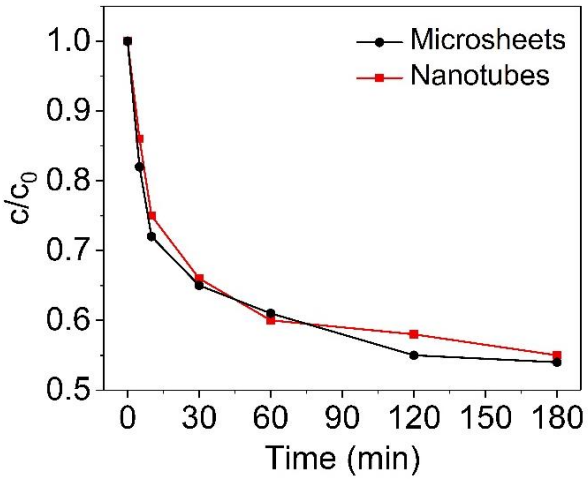

S15. Adsorption of MB by g-C_3N_4 microsheets and nanotubes in dark. The adsorption–desorption equilibriums are established after stirring for three hours. The adsorption abilities of the microsheets and nanotubes are pretty close.

Photodegradation: Photodegradation of MB solution under visible light (λ>420 nm) is conducted in a home-made reactor. An external cooling water circulator was equipped to keep the reactor at a constant temperature. In detail, 50 mg photocatalysts were dispersed into 100 mL MB solution (10 mg L^{-1}), and the suspension was stirred overnight in the dark to ensure the establishment of an adsorption–desorption equilibrium before irradiation. A 300 W xenon lamp with a 420 nm cut-off filter to remove any irradiation below 420 nm was used as the visible light source. At certain time intervals (5 min), the reaction solution was sampled and centrifuged to remove the photocatalysts. The residual MB concentration was determined by the intensity of the absorption peak at 664 nm.

The photocatalytic activity of the g-C_3N_4 nanotubes was evaluated by photodegradation of methylene blue (MB) under visible light (**S 14**). It was found that the photocatalytic activity of g-C_3N_4 nanotubes was obviously improved than that of g-C_3N_4 microsheets. A 100 mL MB solution (10 mg L^{-1}) was almost thoroughly photo-bleached in 55 min by g-C_3N_4 nanotubes, while only ca.80% MB was degraded by the microsheets under the same conditions. The adsorption experiments in dark were conducted to exclude the improved photocatalytic performance of nanotubes is caused by the increased adsorption ability due to the possible large surface area (**S15**).

S16. A comparison of the C_3N_4 nanotubes to the references.

Reference	Size	XRD peak position of (002)	PL	Photocatalytic performance
RSC Adv. 2015, 5, 4026	H12-C_3N_4: diameter: 80 to108 nm; wall thickness: 23 nm	27.8°	PL in the range of 410 nm to 550 nm and centered at ca. 470 nm.	The RhB photodegradation rates for bulk-g-C_3N_4, H12–C_3N_4 and H24–C_3N_4 are 0.005, 0.06 and 0.03 min^{-1}, respectively.
	H24-C_3N_4: diameter: 80 to108 nm, wall thickness: 12 nm	27.7°		
RSC Adv. 2014, 4, 59513	The inner and outer diameters are 150 and 300 nm, respectively.	27.5°	PL in the range of 410 nm to 550 nm and centered at ca. 450 nm	RhB degradation rate is 0.074 min^{-1}. The hydrogen evolution efficiency of is 28.5 mmol h^{-1}
Mater. Lett. 2017, 196, 100	The diameter of the nanotubes is 300–600 nm	27.3°	PL in the range of 410 nm to 550 nm and centered at ca. 420 nm	RhB solution can be degraded completely after the irradiation time of 180 min for tubular g-C_3N_4, which is superior to the bulk g-C_3N_4
J. Mater. Chem. A, 2014, 2, 2885	The wall thickness of the nanotubes is about 15 nm while the inner diameter is about 18 nm.	27.5°	PL in the range of 410 nm to 600 nm and centered at ca. 460 nm	RhB degradation rate: 0.01 min^{-1}
J. Mater. Chem. A, 2017, 5, 12723	Tube wall thicknesses of less than 10 nm	27.4°	PL peak at 462 nm PL lifetime: 15.37 ns	The achieved apparent quantum yield (AQY) of optimal structure for H2 evolution with a green LED (525 nm) reaches 1.3%,
Nanoscale, 2012, 4, 3687	Wall thickness of 20 nm	27.4°	The PL spectra of the C_3N_4 nanotube exhibit a strong emission peak centered at 402 nm	N.A.
Appl. Cata. B: Environ. 2017, 211, 1	Diameters of 0.5–3 μm and lengths of several tens to hundreds micrometers	27.4°	Strong PL emission peak at about 450 nm,	The photocatalytic CH_3OH production rate 0.2 μmol h^{-1} g^{-1}
Chem. Comun. 2004, 1, 26–27	Inner diameters of 50–100 nm and wall thicknesses of 20–50 nm	25°	N.A.	N.A.
This work	The lengths of the nanotubes are about 0.2-2.7 μm. And the diameters span from 20 to 250 nm.	27.5°	PL in the range of 400 nm to 550 nm and centered at ca. 425 nm. Lifetime: long parameter ~10 ns, short parameter ~3 ns.	MB degradation rate is 0.042 min^{-1}

SI Reference

R1 Gan, Z. X.; Liu, L. Z.; Wu, H. Y.; Hao, Y. L.; Shan, Y.; Wu, X. L.; Chu, P. K. Quantum Confinement Effects Across Two-dimensional Planes in MoS_2 Quantum Dots. *Appl. Phys. Lett.* **2015**, *106*, 233113.

R2 Zhao, X.; Ma, X.; Sun, J.; Li, D. H.; Yang, X. R. Enhanced Catalytic Activities of Surfactant-Assisted Exfoliated WS_2 Nanodots for Hydrogen Evolution. *ACS Nano* **2016**, *10*, 2159–2166.

R3 Štengl, V.; Henych, J.; Kormunda, M. Self-Assembled BN and BCN Quantum Dots Obtained from High Intensity Ultrasound Exfoliated Nanosheets. *Sci. Adv. Mater.* **2014**, *6*, 1–11.

R4 Sun, Z. B.; Xie, H. H.; Tang, S. Y.; Yu, X. F.; Guo, Z. N.; Shao, J. D.; Zhang, H.; Huang, H.; Wang, H. Y.; Chu, P. K. Ultrasmall Black Phosphorus Quantum Dots: Synthesis and Use as Photothermal Agents. *Angew. Chem. Int. Ed.* **2015**, *54*, 11526–11530.

R5 Meng, M.; Gan, Z. X.; Zhang, J.; Liu, K. L.; Wang, L.; Li, S. F.; Yao, Y.; Zhu, Y.; Li, J. *Phys. Status Solidi B* **2017**, *254*, 1700011.

R6 Ruan, L. W.; Zhu, Y. J.; Qiu, L. G.; Lu, Y. X. Mechanical Properties of Doped g-C_3N_4 – A First-Principle Study. *Vacuum* **2014**, *106*, 79–85.

R7 Lee, C.; Wei, X. D.; Kysar, J. W.; Hone, J. Measurement of the Elastic Properties and Intrinsic Strength of Monolayer Graphene. *Science* **2008**, *321*, 385–388.

R8 Song, L.; Ci, L. J.; Lu, H.; Sorokin, P. B.; Jin, C. H.; Ni, J.; Kvashnin, A. G.; Kvashnin, D. G.; Lou, J.; Yakobson, B. I.; Ajayan, P. M. Large Scale Growth and Characterization of Atomic Hexagonal Boron Nitride Layers. *Nano Lett.* **2010**, *10*, 3209–3215.

R9 Castellanos-Gomez, A.; Poot, M.; Steele, G. A.; van der Zant, H. S. J.; Agrait, N.; Rubio-Bollinger, G. Elastic Properties of Freely Suspended MoS_2 Nanosheets. *Adv. Mater.* **2012**, *24*, 772–775.

R10 Kaplan-Ashiri, A.; Cohen, S. R.; Gartsman, K.; Rosentsveig, R.; Seifert, G.; Tennea, R. Mechanical Behavior of Individual WS_2 Nanotubes. *J. Mater. Res.* **2004**, *19*, 454–459.

R11 Azofra, L. M.; MacFarlane, D. R.; Sun, C. H. A DFT Study of Planar vs. Corrugated Graphene Like Carbon Nitride (g-C_3N_4) and Its Role in The Catalytic Performance of CO_2 Conversion. *Phys. Chem. Chem. Phys.* **2016**, *18*, 18507–18514.

R12 Gracia, J.; Kroll, P. First Principles Study of C_3N_4 Carbon Nitride Nanotubes. *J. Mater. Chem.* **2009**, *19*, 3020–3026.

R13 Wang, J. X.; Huang, J.; Xie, H. L.; Qu, A. L. Synthesis of g-C_3N_4/TiO_2 with Enhanced Photocatalytic Activity for H_2 Evolution by a Simple Method. *Int. J. Hydrogen Ener.* **2014**, *39*, 6354−6363.

R14 Zimmerman, J. L.; Williams, R.; Khabashesku, V. N.; Margrave, J. L. Synthesis of Spherical Carbon Nitride Nanostructures. *Nano Lett.* **2001**, 1, 731−734.

R15 Liu, S. W.; Chen, F.; Li, S. T.; Peng, X. X.; Xiong, Y. Enhanced Photocatalytic Conversion of Greenhouse Gas CO_2 into Solar Fuels over g-C_3N_4 Nanotubes with Decorated Transparent ZIF-8 Nanoclusters. *Appl. Catal. B: Environ.* **2017**, *211*, 1–10.

R16 Han, Q.; Wang, B.; Gao, J.; Cheng, Z. H.; Zhao, Y.; Zhang, Z. P.; Qu, L. T. Atomically Thin Mesoporous Nanomesh of Graphitic C_3N_4 for High-efficiency Photocatalytic Hydrogen Evolution. *ACS Nano* **2016**, *10*, 2745−2751.

R17 Liang, Q. H.; Li, Z.; Huang, Z. H.; Kang, F.; Yang, Q. H. Holey Graphitic Carbon Nitride Nanosheets with Carbon Vacancies for Highly Improved Photocatalytic Hydrogen Production. *Adv. Funct. Mater.* **2015**, *25*, 6885–6892.

R18 Tu, W. T.; Xu, Y.; Wang, J. J.; Zhang, B. W.; Zhou, T. H.; Yin, S. M.; Wu, S. Y.; Li, C. M.; Huang, Y. Z.; Zhou, Y.; Zou, Z. G.; Robertson, J.; Kraft, M.; Xu, R. Investigating the Role of Tunable Nitrogen Vacancies in Graphitic Carbon Nitride Nanosheets for Efficient Visible-Light-Driven H_2 Evolution and CO_2 Reduction. *ACS Sustainable Chem. Eng.* **2017**, *5*, 7260−7268.

R19 Jiang, J. Z.; Ou-yang, L.; Zhu, L. H.; Zheng, A. M.; Zou, J.; Yi, X. F.; Tang, H. Q. Dependence of Electronic Structure of g-C_3N_4 on the Layer Number of Its Nanosheets: A Study by Raman Spectroscopy Coupled with First-principles Calculations. *Carbon* **2014**, *80*, 213–221.

R20 Zinin, P. V.; Ming, L. C.; Sharma, S. K.; Khabashesku, V. N.; Liu, X. R.; Hong, S. M.; Endo, S.; Acosta, T. Ultraviolet and Near-infrared Raman Spectroscopy of Graphitic C_3N_4 Phase. *Chem. Phys. Lett.* **2009**, *472*, 69–73.

R21 Ni, Z. H.; Yu, T.; Lu, Y. H.; Wang, Y. Y.; Feng, Y. P.; Shen, Z. X. Uniaxial Strain on Graphene: Raman Spectroscopy Study and Band-gap Opening. *ACS Nano* **2008**, *2*, 2301–2305.